Toward an optimal inversion method for synthetic aperture radar wind retrieval

M. Portabella and A. Stoffelen

Royal Netherlands Meteorological Institute, De Bilt, Netherlands

J. A. Johannessen

Nansen Environmental and Remote Sensing Center, Bergen, Norway

[1]   In recent years, particular efforts have been made to derive wind fields over the oceans from synthetic aperture radar (SAR) images. In contrast with the scatterometer, the SAR has a higher spatial resolution and therefore has the potential to provide higher resolution wind information. Since there are at least two geophysical parameters (wind speed and wind direction) modulating the single SAR backscatter measurements, the inversion of wind fields from SAR observations has an inherent problem of underdetermination. Moreover, this modulation is highly nonlinear, further complicating the inversion. *Lorenc* [1986] presented a general statistical approach to solve inversion problems (including underdetermined problems) in meteorological analysis. We propose a SAR wind retrieval method based on this general approach. This simplified method combines the SAR information with some background information coming from high-resolution limited area model to retrieve the most probable wind vector, assuming that all sources of information contain errors and that these are well characterized. We then evaluate two different SAR wind retrieval methods. The first one is commonly used by the SAR community and is based on a combination of a wind streak detection algorithm (wind direction retrieval) and a C band model inversion (wind speed retrieval). The second one is the new method we propose, based on the general statistical approach. We show the potential problems and limitations of using any of these methods and show how the second method can potentially contribute to a significant improvement in SAR wind retrieval. The new method prepares the ground for the assimilation of SAR data in high-resolution numerical weather prediction models.   *INDEX TERMS:* 3220 Mathematical Geophysics: Nonlinear dynamics; 3260 Mathematical Geophysics: Inverse theory; 3329 Meteorology and Atmospheric Dynamics: Mesoscale meteorology; 3360 Meteorology and Atmospheric Dynamics: Remote sensing; *KEYWORDS:* SAR, inversion theory, nonlinearity, underdetermination problem, mesoscale winds

1.   Introduction

[2]   The synthetic aperture radar (SAR) backscatter intensities ($\sigma°$) and their statistical properties contain quantitative information about the state of the sea surface roughness. This, in turn, can be used to derive estimates of the integrated mixture of processes and features in the upper ocean and in the atmospheric boundary layer [*Alpers*, 1995; *Johannessen et al.*, 1991]. Moreover, from the form and the location of the roughness pattern, one can, in the majority of cases, determine unambiguously whether it arises from predominantly oceanic or atmospheric processes and features [*Johannessen et al.*, 1996; *Alpers et al.*, 1998].

[3]   C band SAR images of the sea surface usually manifest expressions of atmospheric phenomena occurring in the marine boundary layer. Most common among these phenomena are boundary layer rolls, atmospheric convec-

tive cells, atmospheric internal gravity waves, tropical rain cells, katabatic wind flows, and meteorological fronts. This has recently been documented in a series of papers published in the special section on Advances in oceanography and sea ice research using ERS observations (*J. Geophys. Res., 103*(C4), pp. 7753–8213, 1998) (hereinafter referred to as JGR98) and in an issue of the *Earth Observation Quarterly* (*59*, 1998) (hereinafter referred to as EOQ98).

[4]   Although much work has been done on the forward modeling of estimating the radar backscatter modulations from the geophysical parameters, there are fewer reports on inverse modeling to estimate geophysical parameters from the $\sigma°$ modulations. The main reason for this comes from the fact that several geophysical phenomena are causing radar backscatter variations. Thus single backscatter measurements over the ocean may not be uniquely related to a particular geophysical condition (underdetermination problem). In addition, the relationship between $\sigma°$ and geophysical parameters is ambiguous and nonlinear, further complicating the inversion.

[5] Scatterometer observations over the ocean provide direct estimates of the global wind vector field with a spatial sampling of 25 km and accuracy of 3 m s^{-1} in the wind vector [*Stoffelen and Anderson*, 1992]. In contrast, the SAR achieves a finer spatial resolution and therefore has the potential to provide wind field information with much more spatial detail. This can be important in a number of applications, such as in semienclosed seas, in straits, along marginal ice zones, and in coastal regions, where scatterometer measurements are contaminated by backscatter from land and ice and the wind vector fields are often recognized to be highly variable [*Johannessen et al.*, 1991]. In such regions, wind field estimates retrieved from SAR images would be very desirable.

[6] Local wind fields, such as land-sea breezes and katabatic wind flows, strongly affect the microclimate in coastal regions. They determine, to a large extent, the advection and dispersion of pollutants in the atmosphere and coastal waters (by generation of local wind driven currents). Since most of the world's population lives in coastal areas and most pollutants are released into the environment near coasts, the study of these local winds is also of great relevance for environmental purposes.

[7] The optimum way to extract information from SAR images is to combine them with in situ measurements and/or mesoscale numerical models [*McNider and Pielke*, 1984; *Gudiksen et al.*, 1992]. However, in situ measurements, i.e., buoys, are often too coarse and far in distance from SAR acquisitions [*Fetterer et al.*, 1998], leading to uncertainties or errors in the results. In contrast, the collocations with mesoscale numerical weather prediction (NWP) model data can be precisely performed both in space and time. However, generally, the resolution of these mesoscale models is too coarse, primarily due to lack of observations. Nevertheless, the atmospheric boundary layer conditions, including the wind vector field derived from NWP models, may be combined with SAR observations at fine spatial resolution to more fully determine and characterize the detailed conditions of the atmosphere–ocean boundary layer.

[8] In this paper we will therefore investigate how the use of SAR data can improve the quantitative description of the mesoscale wind field in coastal regions. In so doing, we will examine several SAR wind retrieval methods with the aim of obtaining the optimum wind field retrieval based on integrated use of SAR and high-resolution limited area model (HIRLAM) data.

[9] The data used in this study are presented in section 2. Some of the current SAR wind retrieval algorithms are discussed in section 3, together with a generalized inverse method using Bayesian probability analysis. In section 4 an examination of two different SAR wind retrieval methods is performed. Finally, the conclusions are presented in section 5.

2. SAR and HIRLAM Data

[10] The second European Remote Sensing Satellite (ERS-2) carries a SAR that operates at a radar frequency of 5.3 GHz (C band), transmits and receives the radar signals at vertical polarization, and has a right-looking antenna that illuminates the Earth's surface at a mean incidence angle of 23°. A set of 15 SAR images that were

Table 1. Selected ERS-2 PRI Single Aperture Radar (SAR) Images

Orbit	Frame	Acquisition Date	Acquisition Time, UTC	Wind Conditions[a]
9381	2529	4 Feb. 1997	1048:56	H/Off
9567	2511	17 Feb. 1997	1040:04	M/Along
9610	2547	20 Feb. 1997	1046:20	M/Off
10297	2511	9 April 1997	1037:13	L/Along
10569	2547	28 April 1997	1040:34	M/On
10984	2511	27 May 1997	1028:37	M/On
11428	2511	27 June 1997	1054:30	H/Along
11614	2547	10 July 1997	1046:23	L/Along
12072	2547	11 Aug. 1997	1040:37	L/Off
12301	2511	27 Aug. 1997	1037:14	L/Off
12430	2511	5 Sept. 1997	1054:28	M/Off
12487	2511	9 Sept. 1997	1028:35	H/On
12530	2511	12 Sept. 1997	1034:19	M/Along
12931	2511	10 Oct. 1997	1054:29	H/Off
12988	2511	14 Oct. 1997	1028:37	L/On

[a]L, low winds (<7 m s^{-1}); M, medium winds (7 m s^{-1} < v < 13 m s^{-1}); H, high winds (>13 m s^{-1}); On, onshore winds; Off, offshore winds; Along, alongshore winds.

acquired from January 1997 to October 1997 by the ERS-2 over the southern North Sea coastal regions were selected, representing various wind conditions (onshore, offshore, along-shore, low, medium, and high). The ERS-2 SAR images presented in this paper are precision images (PRI) provided by the European Space Agency (ESA) [*Grabak and Laur*, 1995]. All SAR acquisition times are between 1000 and 1100 UTC. The selected SAR images are listed in Table 1.

[11] HIRLAM V55, a high-resolution (55 km) mesoscale NWP model, is run operationally at the Royal Dutch Meteorological Institute (KNMI). It has the capability of running a nested very high resolution (VHR) model with a 5-km resolution, which is able to simulate and generate specific mesoscale atmospheric weather phenomena, such as land-sea breezes [*De Bruijn*, 1997]. This model yields as output, among other things, the wind field at 10 m height above the sea surface, which can be compared to or combined with the near-surface wind information inferred from the SAR images.

[12] Both the V55 and the VHR models have a rotated regular latitude-longitude grid with the South Pole at (30°S, 180°E) and are encoded on an Arakawa C grid [*Mesinger and Arakawa*, 1976], meaning that wind vector components (u and v) and temperature (T) are staggered in the horizontal. In the vertical plane a hybrid p-σ coordinate system is used that is nonorthogonal and terrain following. In total, there are 31 vertical levels, six of them in the atmospheric boundary layer, below a height of 2000 m. The lowest level is above 100 m. In order to provide the 10-m-level wind field in the model output, extrapolations from the lowest 100-m level are performed using a boundary layer model that takes into account the stratification. Both a fourth-order explicit linear diffusion and a Eulerian advection scheme are used as default in the models. The analysis is performed on the V55 model. The nested model does not have its own analysis scheme and receives its initial information from the coarse mesh model. There are no specific physical parameterization schemes for the VHR model. A complete description of these schemes is given by *Gustafsson* [1991].

[13] The integration area of the VHR model is fixed for all simulations and is large enough to avoid boundary effects in the areas where the SAR images have been acquired. The forecast files contain a large number of atmospheric fields (wind, temperature, humidity, etc.) at several levels, from which only the wind field at 10 m high above the sea surface is picked up.

[14] In order to collocate the HIRLAM output product to the calibrated SAR (including analog to digital converter power loss correction) image at a standard size of 80 × 95 km, we define a wind cell in the SAR image as an area of 5 × 5 km only covered by ocean (no land or ice "contamination"). In a pure ocean calibrated SAR image, there are a total of 304 (16 × 19) wind cells. Next, the HIRLAM output product is spatially interpolated to the actual coordinates of the wind cells. Finally, as HIRLAM forecasts are provided on an hourly basis, the HIRLAM outputs are linearly interpolated to the actual acquisition time of the SAR image.

3. Wind Retrieval

3.1. Introduction

[15] In recent years several algorithms have been developed and applied for SAR wind retrievals. Common among these are the CMOD-4 [*Stoffelen and Andersen*, 1992; *Johannessen et al.*, 1994] or the CMOD-Ifremer [*Institut Français de Recherche pour l'Exploitation de la Mer*, 1996] inversion, the SAR wind direction algorithm (SWDA) [*Wackerman et al.*, 1996; *Vachon and Dowson*, 1996; *Fetterer et al.*, 1998], and the SAR wind algorithm (SWA) [*Chapron et al.*, 1995, *Kerbaol et al.*, 1998], which are all empirically based methods. A comprehensive presentation of these methods is given in JGR98 and EOQ98 and by *Fetterer et al.* [1998].

[16] In the C band models, $\sigma°$ is a nonlinear function of wind speed (exponential) and wind direction (harmonic). For the ERS-1 scatterometer (whose data are used to develop the C band models), three $\sigma°$ values are available at each node, allowing a solution of the CMOD-4 inversion to be obtained after taking account of the nonlinearity [*Stoffelen and Anderson*, 1997b]. In contrast, inversion of a single SAR $\sigma°$ measurement is more difficult, as the sensitivity depends on the (unknown) true surface wind vector. One is therefore usually facing ambiguities and a problem of underdetermination.

[17] A limitation of the SWDA is that the spatial resolution of the wind direction information is derived from 25-km averages within the SAR image. Hence, at scales smaller than this, no wind direction information is available. In turn, all the $\sigma°$ variability is incorrectly assigned to wind speed variability, by ignoring potential wind direction variability at these scales. Another problem of the SWDA is the 180° ambiguity in the wind direction determination, which is due to the fact that the wind streak reflects the orientation of the wind but not its sense of direction.

[18] A limitation of the SWA is that the longer waves used to determine the smearing in the SAR image spectrum are not fully coupled to local wind variations. In addition, as the wind waves and swell starts to feel the bottom topography as they move into shallow water, their period remains constant, but their propagation direction changes and the phase speed decreases. In turn, their wavelength decreases as well [*Pond and Pickard*, 1978]. This leads to an underestimation of the SWA wind retrievals. Similar difficulties arise for offshore winds, in particular in shallow water, as the fetch and depth-limited waters affect the growth of the wave spectrum. As, for a given wind speed, it never reaches the spectrum for fully developed seas, the SWA retrieval will underestimate the wind speed. Since the present study is focused on shallow water regions (mostly 100 m depth or below), the wind field retrieval based on the SWA algorithm has been discarded.

[19] We have chosen to apply SWDA and CMOD-4 inversion for further examination of the limitations addressed above. The algorithms are therefore briefly introduced below.

3.1.1. SAR wind direction algorithm

[20] The SWDA is used to extract the wind direction information from linear, low-frequency expressions detected in the SAR image. These are usually associated with wind rows or wind streaks, which are manifestations of roll vortices in the planetary boundary layer (PBL) [*Brown*, 1990; *LeMone*, 1973]. The rolls are approximately aligned with the surface wind. Roll vortices in the PBL are counter-rotating helical circulations that are superimposed on the dominant wind field. They are most pronounced during unstable conditions [*Wackerman et al.*, 1996], although *Etling and Brown* [1993] reported the presence of wind rolls in stable conditions, as well. The SWDA was proposed by *Fetterer et al.* [1998] and looks for these linear expressions in the Fourier domain of the SAR image at a spatial resolution of 25 km to determine wind direction. Subsequently, SAR wind speed is usually retrieved at smaller resolution.

3.1.2. C band model inversion

[21] The CMOD-4 model was originally developed for the ERS-1 scatterometer [*Stoffelen and Anderson*, 1993], but it has also been shown to give reasonable estimates of wind speed when applied to ERS SAR images [*Johannessen et al.*, 1994]. The model is based on the backscatter from the rough ocean surface for moderate incidence angles (20°–60°), which is dominated by resonant Bragg scattering [*Valenzuela*, 1978]. Additionally, Rayleigh scattering and specular reflection may contribute to the backscatter.

[22] The CMOD-4 model provides $\sigma°$ values as a function of relative wind direction φ ($\varphi = 0°$ for a wind blowing towards the radar), wind speed v, and incidence angle θ. The relationship can be expressed as

$$\sigma^0 = B_0[1 + B_1 \cos(\phi) + B_2 \cos(2\phi)]^{1.6}. \quad (1)$$

[23] The coefficients B_0, B_1, and B_2 depend on the local incidence angle of the radar beam and the wind speed. The model is tuned to the real ("true") wind at 10-m height and the ERS-1 scatterometer $\sigma°$. CMOD-4 describes the coherence of the forebeam, aftbeam, and midbeam backscatter measurement (the so-called cone surface) within ~0.1 dB. Wind retrieval based on CMOD-4 [*Stoffelen and Anderson*, 1997a] results in an accuracy of 3 m s^{-1} vector root-mean-square (RMS) when applied to scatterometer data [*Stoffelen*, 1998]. Other relevant references here

include work by *Korsbakken et al.* [1998] and *Lehner et al.* [1998].

[24] In order to derive the wind field in a SAR PRI image from a C band model inversion, comprehensive calibration of the radar backscatter value $\sigma°$ is required [*Scoon et al.*, 1996]. The calibration procedure performed in this study is given by *Laur et al.* [1998].

3.1.3. Problem of underdetermination

[25] Besides the limitations of the different algorithms presented in section 3.1, there is a very important problem inherent in SAR $\sigma°$ observations. Both wind speed and wind direction information are present at the same time and cannot be properly discriminated. As discussed previously, this underdetermination problem is obviously present in the wind vector retrieval algorithms, such as CMOD-4. Moreover, it directly affects the quality of the retrievals of the algorithms, which only derive one wind component, such as SWA or SWDA.

[26] A methodology that combines some of these algorithms with some additional information, i.e., NWP models or buoy data, may be the solution to this inherent problem in SAR wind retrieval. In order to be successful, the method should take into account the spatial and accuracy characteristics and limitations of the observations and of the additional data used to combine them in an optimal way.

[27] In section 3.2 we consider an alternative approach by which the problem of underdetermination can be solved in a statistical way. The general statistical approach used by *Lorenc* [1986] to solve inversion problems (including underdetermined problems) in meteorological analysis is first briefly reviewed, followed by a discussion of its potential use for SAR wind field retrievals.

3.2. General Approach

[28] The idea is to combine the SAR information, i.e., $\sigma°$ and/or wind streaks, with some background information, i.e., NWP models and/or buoy data, to retrieve the most probable wind vector, assuming that all sources of information contain errors and that these are well characterized, including their spatial correlation. This approach is used more generally in meteorological analysis. *Lorenc* [1986] proceeded from a completely general Bayesian analysis equation, expressed in terms of multidimensional probability distribution functions, through a fairly standard set of assumptions, to a variational equation for the "best" analysis.

[29] In order to get the best analysis, we first need to know the relationship between the model state $\mathbf{x}$ and the observations $\mathbf{y}$. We assume that this can be represented by an explicit operator k_n such that

$$\mathbf{y} = k_n(\mathbf{x}) \tag{2}$$

is the best estimate of $\mathbf{y}$ for a given $\mathbf{x}$. The operator k_n is the so-called forward model, and the subscript n reminds us that it might be nonlinear. The analysis problem is thus to find the best estimate of $\mathbf{x}$ that inverts equation (2) for a given observation $\mathbf{y}$, allowing for observation errors and other prior information.

[30] Bayes' theorem states that the posterior probability of an event A occurring, given that event B is known to have occurred, is proportional to the prior probability of A,

multiplied by the probability of B occurring given that A is known to have occurred,

$$P(A|B) \propto P(B|A)P(A). \tag{3}$$

[31] This is applicable to the inverse analysis problem. If A is the event true state ($\mathbf{x_t}$) and B is the event observations ($\mathbf{y_o}$), then equation (3) can be rewritten as

$$P(\mathbf{x_t}|\mathbf{y_o}) \propto P(\mathbf{y_o}|\mathbf{x_t})P(\mathbf{x_t}). \tag{4}$$

[32] Equation (4) defines an N_x-dimensional probability distribution function (PDF), which we shall call $P_a(\mathbf{x})$, specifying all we know about the analysis. The best estimate of the state $\mathbf{x_a}$ can be the mean of $P_a(\mathbf{x})$ or the maximum of $P_a(\mathbf{x})$; these are, respectively, the minimum variance and the maximum likelihood estimates of $\mathbf{x_a}$. For a complete solution to the generalized problem, we need to know also the accuracy of $\mathbf{x_a}$; this information is also contained in $P_a(\mathbf{x})$.

[33] The prior probability $P(\mathbf{x_t})$ contains our knowledge about the state $\mathbf{x}$ before the observations are taken. This can be written as the deviations from (or errors of) some background $\mathbf{x_b}$,

$$P(\mathbf{x_t}) = P_b(\mathbf{x} - \mathbf{x_b}). \tag{5}$$

[34] The posterior probability $P(\mathbf{y_o}|\mathbf{x_t})$ contains the uncertainty in the observation, and the forward model and can be written as

$$P(\mathbf{y_o}|\mathbf{x_t}) = P_{of}(\mathbf{y_o} - k_n(\mathbf{x}))$$

$$= \int P_o(\mathbf{y_t} - \mathbf{y_o}) \cdot P_f(\mathbf{y_t} - k_n(\mathbf{x})) \cdot \mathbf{dy_t}, \tag{6}$$

where $\mathbf{y_t}$ are the true observation values, P_o represents the random observational errors, and P_f represents the forward model errors. Therefore, assuming that P_b and P_{of} are independent, i.e., that background errors and observational errors are uncorrelated, equation (4) becomes

$$P_a(\mathbf{x}) \propto P_{of}(\mathbf{y_o} - k_n(\mathbf{x})) \cdot P_b(\mathbf{x} - \mathbf{x_b}). \tag{7}$$

[35] We now need to specify the PDFs P_b, P_o, and P_f. A common assumption, which simplifies the solution, is that errors are Gaussian, i.e., that the PDFs are multidimensional Gaussian functions. In this case, equation (7) can be written as

$$P_a(\mathbf{x}) \propto \exp\left[-\frac{1}{2}\{\mathbf{y_o} - k_n(\mathbf{x})\}^T (\mathbf{O} + \mathbf{F})^{-1}\{\mathbf{y_o} - k_n(\mathbf{x})\} \right.$$

$$\left. -\frac{1}{2}(\mathbf{x} - \mathbf{x_b})^T \mathbf{B}^{-1}(\mathbf{x} - \mathbf{x_b}) \right], \tag{8}$$

where $\mathbf{O}$, $\mathbf{F}$, and $\mathbf{B}$ are the covariance matrices of P_b, P_o, and P_f, respectively.

[36] Assuming Gaussian errors, both the minimum variance and the maximum likelihood estimates are identical.

For the maximum likelihood estimate, we wish to maximize P_a, which is equivalent to minimizing $-\ln(P_a)$,

$$J = \{\mathbf{y_o} - k_n(\mathbf{x})\}^T (\mathbf{O} + \mathbf{F})^{-1} \{\mathbf{y_o} - k_n(\mathbf{x})\}$$

$$+ (\mathbf{x} - \mathbf{x_b})^T \mathbf{B}^{-1} (\mathbf{x} - \mathbf{x_b}), \tag{9}$$

where J is the so-called cost function and the first and second terms on the right-hand side of equation (9) refer to observation and background terms, respectively.

[37] In case of a nonlinear forward model (K_n) or in case of nonlinear error properties, for example, the error magnitude depending on the value of the true observation, the maximum likelihood solution may have some unwanted features, such as biases [see e.g., *Stoffelen and Anderson*, 1997a]. In these cases it is important to carefully investigate whether the best estimate comes from a minimum variance, a maximum likelihood, or an unbiased analysis objective function [*Stoffelen*, 2000].

3.2.1. SAR application

[38] For SAR, $\mathbf{y_o}$ can contain σ°, wind direction from wind streaks, or other derived parameters (see section 4); k_n can be the C band model, the SWDA, or other SAR wind retrieval algorithm (see section 4); $\mathbf{x_b}$ can be a NWP wind field or buoy wind data; and $\mathbf{x}$ is the wind field at 10-m height. The matrices $\mathbf{O} + \mathbf{F}$ and $\mathbf{B}$ can be diagonal, in which case the global minimization problem is just a sum of local minimization problems. In meteorological analyses, $\mathbf{B}$ is constructed generally from so-called spatial structure functions that provide the spatial error correlation of the background field. Since the observational network is generally rather sparse, the typical correlation length used for wind parameters is 250 km. Except in specific cases of katabatic flow, land breeze, etc. that may provide a well-determined physical forcing, the sparsity of the observation network is also a problem for high-resolution models, such as HIRLAM VHR. Therefore, generally, over a SAR scene the NWP output will be quite smooth.

[39] Also, the $\mathbf{O}$ matrix may contain correlation. A good example is the case where SAR image wind streaks are used for wind direction determination (see section 4). A spatial context of 25 km is used for this [*Fetterer et al.*, 1998], and if the wind state from SAR at, let's say, 5-km resolution is sought, then the contribution from the wind streak observations is spatially correlated.

[40] For SAR, several existing wind retrieval methods can be described by the above formalism. Generally, further simplifying assumptions have to be made, such as $\mathbf{B} \rightarrow \infty$ or $\mathbf{O} + \mathbf{F} = \mathbf{I}$ (identity).

4. Evaluation of Two SAR Wind Retrieval Methods

[41] In this section we evaluate the outcome of two different SAR wind retrieval methods. The first one is based on a commonly used combination of the SWDA and C band models, whereas the second one is the new method based on the generalized inverse approach addressed in section 3.2. This new method, called the statistical wind retrieval approach (SWRA), combines the SAR-derived wind information with the VHR output to determine the optimum

wind vector, using a simplified set of assumptions. Unlike the other methods, this method takes into account the relative quality of the observations (SAR) and the background information (VHR).

4.1. SWDA + C Band Method

[42] In this section we explore a common way of deriving wind vectors based on a combination of one of the C band models and the SWDA, with the additional help of the VHR HIRLAM wind direction information.

4.1.1. Methodology

[43] As described by *Fetterer et al.* [1998], the SWDA is used to retrieve the wind direction from the streak features in the SAR image, which are approximately aligned in the direction of the surface wind. As emphasized in section 3.1, the retrieval method only provides an estimate of the wind streak direction, and therefore a 180° ambiguity remains. In contrast with *Fetterer et al.* [1998], who use buoy data to provide the additional information needed to solve this ambiguity, we use the VHR model; that is, the direction value closest to that given by the VHR is selected.

[44] The SWDA provides wind direction information in 25-km grid cells. In order to retrieve a wind vector of 5-km resolution (VHR model resolution), the 25-km cells are subdivided into 5-km wind cells, assuming a constant and error-free wind direction within the 25-km area. The CMOD-4 is then used to retrieve the wind speed at each wind cell based on the σ°, the incidence angle, and the SWDA wind direction information. We computed wind speed in an area of 3×3-25 km grid cells at 5-km resolution.

[45] As noted in section 3.2, the SAR wind retrieval methods can be described by the general approach, while varying the set of assumptions. Therefore, this alternative method can also be described following the general approach, but with a very strong set of assumptions, notably, no errors and no background term in the cost function.

4.1.2. Validation procedure

[46] Although the quantitative validation is done with the VHR model wind information as a reference, a method based on an optimum combination of both VHR and C band models is also used to qualitatively analyze some specific cases. In so doing, one can alternatively retrieve the wind speed or the wind direction from the C band model, using the VHR wind direction or wind speed products as input. In the latter case, when wind direction is retrieved, four ambiguities are generally found from which the closest to the VHR direction is selected. The RMS difference of the retrieved wind vector component compared to the VHR component can then be estimated.

$$\mathrm{RMS} = \sqrt{\frac{\sum\limits_{i=1}^{N} (v_i - v_i^t)^2}{N}}, \tag{10}$$

where v_i and v_i^t correspond to the wind vector component for a particular wind cell provided by the C band and the VHR models, respectively, and where N is the number of wind cells in the SAR image.

[47] The method, described by *Portabella* [1998], uses variations around the input VHR values to look for the

minimum RMS. In the case of wind speed retrievals, the variations are performed in the VHR wind direction, looking for a minimum RMS in wind speed; similarly, in the case of wind direction retrievals, the variations are performed in the VHR speed field, looking for a minimum RMS in wind direction. These two fields are based on the independent sensitivities to direction $\left(\frac{\partial \sigma^\circ}{\partial \Phi}\right)_f$ and speed $\left(\frac{\partial \sigma^\circ}{\partial f}\right)_\Phi$ changes, respectively (where f is wind speed and Φ is wind direction). As the VHR wind fields are smooth, the method therefore assumes that all the variability captured in the SAR image is assigned to either the wind speed component (for wind speed retrievals) or the wind direction component (for wind direction retrievals).

4.1.3. Validation

[48] The combination of wind streak detection and C band models is widely used to quantify wind field in SAR images. *Fetterer et al.* [1998] obtained a RMS difference (compared to buoy data) of 2 m s^{-1} in wind speed and 37° in wind direction using this combined method in a total of 61 ERS-1 SAR PRI images.

[49] In this section we will focus our attention on the potential use of this method and its weaknesses, rather than performing a full validation. For this purpose, we have chosen two SAR images out of the set of 15. These images present clearly visible wind streaks. Figures 1a and 2a show the SAR image, Figures 1b and 2b show the corresponding VHR wind field, Figures 1c and 2c show the CMOD-4 retrieved speeds at fixed (or VHR shifted) directions, Figures 1d and 2d show the CMOD-4 retrieved directions at fixed (or VHR shifted) speeds, and Figures 1e and 2e show the SWDA + CMOD-4 wind field for the two SAR scenes. The validation results are summarized in Table 2.

4.1.3.1. Case 1

[50] The VHR model predicted a mean speed of 6.2 m s^{-1} and a mean direction of 206.6°. The SWDA derived mean direction field is 231.9° with a RMS difference (compared to the VHR direction field) of 27.9°. Figure 1a shows the wind streak pattern (straight white lines) and the wind fronts (curved white lines) in the SAR image. Examining the wind direction field in Figure 1e, it is clearly discernible that the SWDA successfully detected the wind streaks in the image, except for the lower right corner where there is no clear pattern of wind streaks. There is a bias of 25.3° toward crosswind of the retrieved directions compared to the VHR directions (see Figures 1b and 1e), suggesting that the wind streaks may not be perfectly aligned with the true wind direction. *Wackerman et al.* [1996] and *Alpers and Brummer* [1994] reported that the wind streaks are aligned in a direction slightly to the right or to the left of the true direction. This bias depends on the roll generation mechanisms (dynamic or convective instabilities), the strength of the PBL stratification, and the vertical velocity profile of the PBL [*Gerling*, 1986]. Note the unrealistic wind direction block structure in Figure 1e, with wind speed jumps associated with the arbitrary shift in wind direction. This is caused by the fact that the resolutions of the wind speed and wind direction determination do not match.

[51] The CMOD-4 derived mean wind speed field is 5.1 m s^{-1} with a RMS difference of 1.7 m s^{-1}. It is discernible from Figure 1e that in the areas where the wind direction estimates are biased toward crosswind compared to VHR directions (Figure 1b), wind speed estimates are high compared to VHR speeds. This documents, as expected, that C band model errors are directly affected by the errors in the direction estimation; that is, a direction bias toward crosswind will produce an overestimation of C band wind speeds, and a bias toward upwind or downwind will produce underestimation in the C band speeds.

[52] Despite this bias, the wind speed field retrieved from the C band model suggests the presence of wind fronts, which are not detected by the VHR model. The upper right corner of Figure 1e corresponds to the higher wind speed part of the front ($\sim$8 m s^{-1}). In the lower left corner of Figure 1e there is also an increase of the wind speed, suggesting the presence of a second, somewhat weaker front. This is also the case for the retrieved wind speeds at fixed directions in Figure 1c, where the fronts can be seen as a wind speed change. In comparison, the retrieved wind direction at fixed speed (Figure 1d) also shows the wind front, but by a change in wind direction. According to the wind streak information, Figure 1c is more realistic than Figure 1d, although it is likely that both retrieval methods contain errors due to the strict assumptions of σ° variability as either wind speed or wind direction variations.

4.1.3.2. Case 2

[53] The VHR model predicted a mean speed of 12.6 m s^{-1} and a mean direction of 322.9°. The SWDA mean direction field is 323.9° and the RMS difference is 16.5°. Figure 2a shows the wind streaks (straight lines) in the SAR image. Although there is no significant bias in this case, the image presents some variability in the wind direction. In particular, the wind streaks are changing direction in the right part of the image (straight black lines), suggesting the presence of a wind front (curved black line), which is not predicted by the VHR model. To the left of the front, the wind streak directions are biased $\sim$15° toward upwind when compared to the VHR directions (see Figures 2b and 2e). This is due to the fact that the precision of the SWDA is affected by the sampling of the SAR scene in the Fourier domain. *Fetterer et al.* [1998] reported that the precision of the direction estimate decreases as the location of the peak gets closer to the origin of the Fourier domain. In particular, for wind streaks with a spacing from 4.5 to 6 km, an angle precision up to 27° was reported. In the lower left corner of the SAR image (Figure 2a) the wind streak spacing is 4.5 km, leading to a discretization of 27° in the wind streak direction determination. Note again the arbitrary blocked structure of the wind field.

[54] The CMOD-4 derived mean speed field is 10.7 m s^{-1}, and the RMS is 2.8 m s^{-1}. The relatively high RMS value indicates a significant variability due to the presence of the wind front. The wind direction field in the right part of the wind front (Figure 2e) is slightly biased toward crosswind compared to the C band retrieved directions at fixed speeds in Figure 2d. On the other hand, the C band retrieved speeds at fixed directions in Figure 2c decrease at right side of the front. Therefore the increase in wind speed to the right of the front (2–3 m s^{-1} higher than the left part) in Figure 2e is mainly due to a misalignment of the wind streaks with respect to the true direction field. In the lower left corner of the image (Figure 2e) the speeds are higher than in the surrounding 25-km wind direction grid cells. This is caused by the error in the wind direction estimation due to the streak spacing. This error is biasing the direction
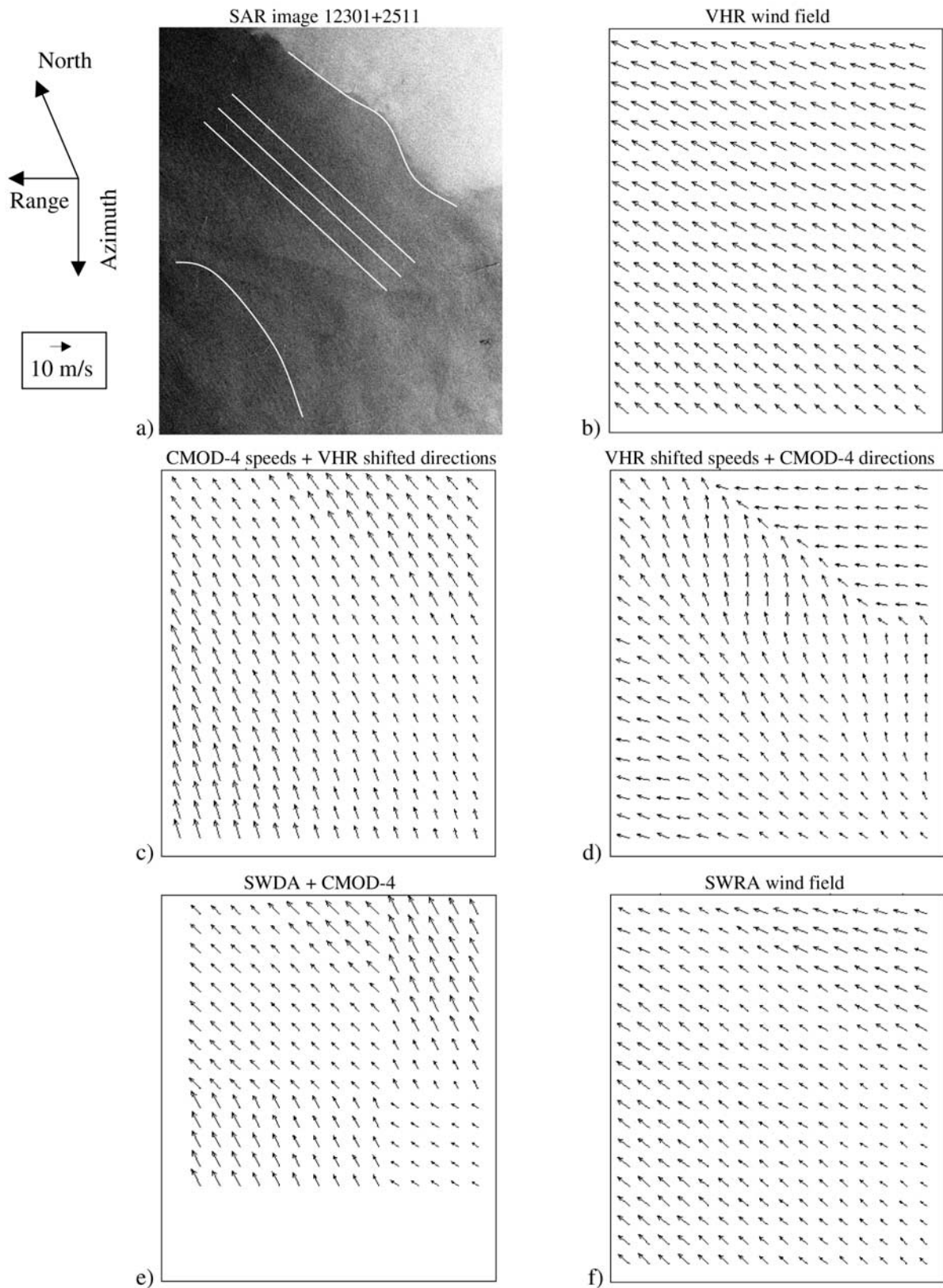
Figure 1. (a) Calibrated SAR image 12301 + 2511. (b) VHR wind field. (c) CMOD-4 speeds from VHR directions shifted 35°. (d) CMOD-4 directions from VHR speeds shifted -1.5 m s^{-1}. (e) CMOD-4 speeds from SWDA directions. (f) SWRA wind field.
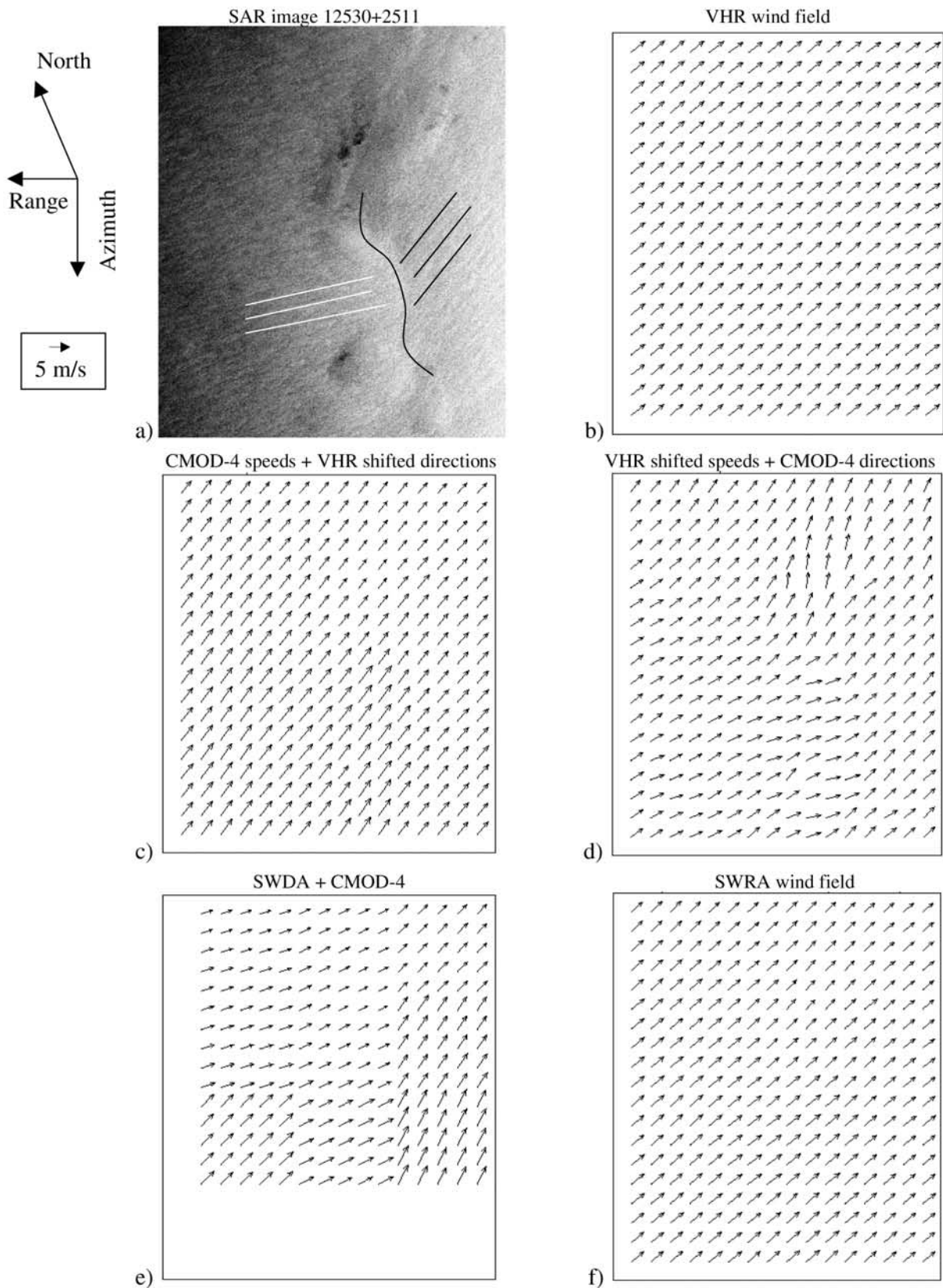
Figure 2. (a) Calibrated SAR image 12530 + 2511. (b) VHR wind field. (c) CMOD-4 speeds from VHR directions shifted $-15°$. (d) CMOD-4 directions from VHR speeds shifted -1.5 m s^{-1}. (e) CMOD-4 speeds from SWDA directions. (f) SWRA wind field.

Table 2. Validation SWDA + CMOD-4

SAR Scene	Very High Resolution HIRLAM Mean Speed, m s^{-1}/Direction, °	Root-Mean-Square in Speed, m s^{-1}/Direction, °	Bias in Speed, m s^{-1}/Direction, °
Case 1	6.2/206.6	1.7/27.9	−1.1/25.3
Case 2	12.6/322.9	2.8/16.5	−1.9/1

toward crosswind in this particular 25-km cell, which in turn produces higher C band retrieved wind speeds than in the surrounding 25-km cells.

[55] In contrast to the previous image (case 1), the retrieved directions at fixed speeds (Figure 2d) are more realistic than the retrieved speeds at fixed directions (Figure 2c), according to the wind streak information.

4.1.3.3. Summary of all cases

[56] In summary, in the set of 15 SAR images, only four contained clear wind streaks and were therefore used to examine the combined SWDA + C band method. The two cases not shown present similar problems to the two cases discussed above, although there is slightly better agreement with the VHR, as no fronts are present in the scenes. This retrieval method is able to detect some atmospheric phenomena, like wind fronts, which are not predicted by the VHR model. However, the accuracy of the SWDA decreases with the wind streak spacing, and, indeed, the wind streaks show some misalignment with the true wind direction. The C band model errors are directly affected by the errors in the direction estimation. Because of the low resolution of the direction retrievals, all the variability in the 25-km cells is assumed to be in the speed component, which is obviously incorrect. Finally, the direction of the local wind is not always detected, hence limiting the full use of the method. We further investigate these cases in section 4.2.

[57] (Note that in this analysis we have used the "peak" method to retrieve wind directions. This method simply finds the position with the highest value and assumes that this represents a peak in the spectrum due to wind streaks. Direction is assumed to be normal to the peak direction. However, *Fetterer et al.* [1998] also used a more sophisticated method to look for the wind direction in the Fourier domain. This second method is called the "cigar-shaped" method and assumes that the wind direction is manifested in the spectrum as a smear of energy in the crosswind direction. This method was reported to be very useful, as it was able to detect not only wind streaks, but also other manifestations of the local wind. Surfactant streaks (at low wind speed), blowing foam and water from breaking waves (at high wind speed), and ellipticity of atmospheric convective cells will give rise to image expressions that are aligned with the local surface wind direction. This, in turn, will generate smears in the "cigar-shaped" spectrum. *Fetterer et al.* [1998] detected smears in the spectrum in all 61 ERS-1 SAR images examined.

4.2. Statistical Wind Retrieval Approach

[58] As explained in section 3.2, the method derived from the general approach will depend on the set of assumptions we make. Here we present a simplified statistical method consisting of combining SAR data and VHR wind to retrieve an optimum wind vector. In contrast with section 4.1, this method assumes that both the SAR obser-

vations (including the retrieval algorithms) and the VHR model output contain errors.

4.2.1. Methodology

[59] The method uses a C band model function as forward model to relate the SAR measured (and calibrated) backscatter to the wind state and uses the VHR wind field as background information.

[60] Therefore equation (9) can be written as

$$J = \{\sigma_m^\circ - \mathrm{CMOD}(\mathbf{v})\}^T (\mathbf{O} + \mathbf{F})^{-1} \{\sigma_m^\circ - \mathrm{CMOD}(\mathbf{v})\}$$

$$+ (\mathbf{v} - \mathbf{v_H})^T B^{-1} (\mathbf{v} - \mathbf{v_H}), \qquad (11)$$

where σ_m° are the backscatter measurements, CMOD is the C band model function, $\mathbf{v_H}$ is the HIRLAM VHR wind field, and v is the wind field estimate.

[61] For simplicity, we assume that there is no spatial correlation ($\mathbf{O} + \mathbf{F}$ and $\mathbf{B}$ are diagonal matrices), and therefore the global minimization problem can be treated as a sum of local minimization problems. In other words, we can minimize the cost function J for every 5-km wind cell, instead of minimizing the entire SAR scene. Therefore, for every wind cell, the cost function we have to minimize is

$$J = \left(\frac{\sigma_m^\circ - \sigma^\circ}{\Delta\sigma}\right)^2 + \left(\frac{\mathbf{v_H} - \mathbf{v}}{\Delta\mathbf{v}}\right)^2, \qquad (12)$$

where σ° is the backscatter value computed by applying the C-band model with the wind vector estimate v and incidence angle θ corresponding to that particular wind cell [$\sigma^\circ = \mathrm{CMOD}(\mathbf{v})_\theta$]; $\Delta\sigma$ and $\Delta\mathbf{v}$ are the Gaussian error Standard Deviations (SDE) from the $\mathbf{O}$ and $\mathbf{B}$ matrices respectively. For simplicity, the forward model has been considered perfect ($\mathbf{F} = 0$).

[62] Assuming that the wind vector component errors are independent, equation (12) can be written as

$$J = \left(\frac{\sigma_m^\circ - \sigma^\circ}{\Delta\sigma}\right)^2 + \left(\frac{u_H - u}{\Delta u}\right)^2 + \left(\frac{v_H - v}{\Delta v}\right)^2, \qquad (13)$$

where u and v are the wind vector components. In order to simplify the discussion of the results, the first term on the right-hand side (in the cost function) of equation (13) will be referred to as the SAR term and the second and third terms on the right-hand side of equation (13) together will be referred to as the VHR term. Following the maximum likelihood estimate method described in section 3.2, the optimum wind vector estimate for any given wind cell will therefore correspond to a minimum in the cost function of equation (13).

[63] The SWRA is based on a scanning approach. A wide range of wind vector values (step size of 0.25 m s^{-1} in both u and v components) around the VHR wind vector value for a particular wind cell are used as "trial" winds in the cost function. Each simulated trial wind (u, v) is inverted (using the C band model functions) to provide a simulated trial radar backscatter (σ°). The simulated trial wind vector (u^i, v^i) that minimizes the cost function J is considered the optimum wind vector for that particular wind cell. Figure 3 shows a conceptual illustration of the SWRA. The solid arrow represents the VHR wind vector for a particular wind
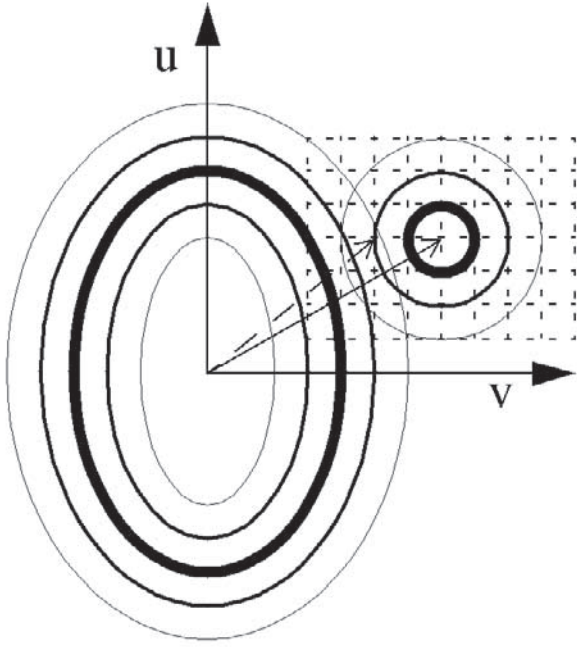
Figure 3. Conceptual illustration of statistical wind vector approach.

cell, and circles around the arrow represent the VHR probability distribution of being the true wind (each circle is a probability "isoline," with probability increasing with isoline thickness). The ellipses around the axis origin are the SAR wind retrieval probability isolines (the spacing between isolines may vary with wind direction due to the different model sensitivities), and the squared grid of dotted lines represents the simulated trial winds where the SWRA is computed. The dashed arrow represents the optimum wind vector, which is given by the minimum value of the cost function (maximum probability).

[64] The Gaussian error stochastic differential equations are chosen following *Stoffelen and Anderson* [1997a]. They reported that choosing a $\Delta\sigma$ proportional to the trial backscatter while looking for a minimum in the cost function leads to a first-order error due to the high nonlinearity in the cost function gradient. Therefore $\Delta\sigma$ will be proportional to the radar backscatter measurement and not to the trial backscatter. As we are looking for the $\Delta\sigma$ in the averaged backscatter over a 5×5 km wind cell, this value should be closely associated with the variability in the backscatter measurement (instrument error plus geophysical error) from 0 to 5 km (subcell variability). The subcell averaged mean SDE for all 15 of the set of SAR images is 7.8% [see *Portabella*, 1998] and is used as the proportionality constant; that is, $\Delta\sigma = 0.078 \, \sigma_m^\circ$.

[65] Δu and Δv represent the error of HIRLAM at 5-km resolution. At present, no attempt has been made at calculating these errors, and since HIRLAM is close to the European Centre for Medium-Range Weather Forecasts (ECMWF) model, we use the ECMWF errors instead. *Stoffelen* [1996] reported a large-scale (250 km) error variance in both ECMWF wind components (u, v) of ~ 1 m^2 s^{-2}. *Stoffelen and Anderson* [1997a] use a climatological wind spectrum to estimate the small-scale variability.

They find that the computed variabilities are consistent with differences between measurement systems with different resolution, i.e., buoys, scatterometer, and ECMWF model. Using their climatological spectrum, we estimate the variability between 5 and 250 km to be 2.0 m^2 s^{-2}, leading to a final total error variance of 3 m^2 s^{-2} in both wind components. Therefore $\Delta u = \Delta v = \sqrt{3}$ m s^{-1}.

4.2.2. Results

[66] Table 3 shows the averaged variability in both wind components (the wind direction variability is given in equivalent meters per second) for all the VHR, SWRA, and C band retrieved wind fields. The latter is computed by using a VHR wind speed (direction) as input to retrieve the wind direction (speed) with the C band model.

[67] The variability in the C band retrieved winds fields is, as expected, much higher than the variability in the VHR wind fields, due to the impact of short-scale atmospheric phenomena that are not included in the VHR model. The fact that the VHR model does not have its own analysis scheme, that it receives its initial information from the V55 model, and that there are no specific parameterization schemes for the VHR model makes the VHR effective resolution closer to 55 km than to 5 km.

[68] Similarly, Table 3 show low variability in the SWRA wind directions, comparable to the variability in the VHR wind fields and much lower than the variability in the C band models retrieved wind directions. On the other hand, the variability in the SWRA wind speeds is between the low variability of the VHR speeds and the higher variability of the C band retrieved speeds. For small-scale turbulence, as depicted in SAR images, one may expect the same amount of variability along and perpendicular to the mean flow (i.e., in the speed and direction components). VHR contains the large scales (~ 100 km), and the SAR term is effective in adding smaller scale (5 km) variability when a discrepancy occurs. This variability is added to the component with largest sensitivity in the C band model, i.e., generally, the speed component.

[69] Figure 1f shows the SWRA wind field for case 1. As discussed in section 4.1.3, Figure 1a shows a SAR image where there are two fronts, which are not predicted by the VHR model (Figure 1b). Figure 1f shows the wind speed change originated by this wind front (upper right and lower left corners). The SWRA wind speeds are between the VHR speeds (Figure 1b) and the CMOD-4 retrieved speeds (Figure 1c), although much closer to the latter, which is also detecting the wind fronts. This is an example where the SWRA has successfully combined both SAR and VHR speed information.

[70] Figure 2f shows the SWRA wind field for case 2. As discussed in section 4.1.3, Figure 2a shows a SAR image where there is a direction change (straight lines) originated by a wind front (curved line), which is not predicted by the

Table 3. Averaged Standard Deviation (STD) Comparisons

Wind Component	VHR Averaged STD	SWRA Averaged STD	CMOD-4 Averaged STD
Speed, m s^{-1}	0.55	0.75	1
Direction, m s^{-1a}	0.45	0.45	1.65

[a] Direction values are given in equivalent meters per second.

VHR model (Figure 2b). This wind direction change, which is clearly reflected in the C band retrieved directions (Figure 2d), is not detected by the SWRA (Figure 2f). This is an example where the SWRA has failed to combine both SAR and VHR direction information. The ad hoc assumption that all observed σ° variations are caused by wind direction (Figure 2d) seems to work better here than considering wind speed and direction sensitivities properly (Figure 2f).

[71] Table 4 shows the ratio of sensitivity of C band model functions to speed and to direction changes,

$$\left(\frac{\partial \sigma^\circ}{\partial f}\right)_\Phi \bigg/ \left(\frac{\partial \sigma^\circ}{\partial \Phi}\right)_f,$$

and the SWRA bias (with respect to VHR) and variability in speed and direction for these two cases. At the speed and direction ranges of the VHR wind field, the sensitivity to speed changes is 2.5 (case 1) and 1.8 (case 2) times larger than the sensitivity to direction changes. As a consequence, the variability is mainly added to the wind speed component, and the bias in wind direction is small compared to the bias in wind speed in both cases (see Table 4). Moreover, the results of the SWRA, not just for these two cases but for the entire set of SAR images, show small variability in the wind direction compared to the wind speed field (see Table 3). Similarly, the overall results of the SWRA show little bias in the wind direction field (mean absolute value of 0.6 equivalent meters per second) compared to the bias in the wind speed field (mean value of -1.5 m s^{-1}). The bias in wind direction is very small in low wind speed cases and especially in the upwind, downwind and crosswind cases. This is, again, because the sensitivity to direction changes is in general too low, and therefore the SAR term has a very broad minimum. The broader the minimum in the SAR term is, the closer the SWRA direction will be to the minimum in the VHR term, which in turn is the VHR direction. This is reasonable, as no "new" information from SAR is provided. As a consequence, wind direction is less well determined than wind speed and thus more uncertain.

[72] In summary, it seems that the SWRA is successfully combining the SAR and the VHR speed information. In comparison, it is systematically adding less variability to the wind direction, biasing the results toward the VHR direction information, since the SAR radar backscatter is generally most sensitive to wind speed variations.

[73] Using the information on wind streaks, one may conclude that the backscatter variability in Figure 2a is caused by the wind direction rather than by the wind speed changes. In order to improve the SWRA performance, an additional wind streak term may be added after investigation of its weight (additional terms in matrix $\mathbf{O} + \mathbf{F}$) as a measure of the quality of the SAR-derived wind direction. Improved wind direction determination will result in improved wind speed retrieval. Furthermore, in meteorological analysis, spatial correlation patterns (matrix $\mathbf{B}$) are used to prescribe the amount of rotation and divergence in the analyzed field. We anticipate that the dominating rotational part would constrain the solution of the SWRA in the appropriate direction. However, we did not test this.

Table 4. Validation SWRA

SAR Scene	Sensitivity Ratio	SWRA STD in Speed, m s^{-1}/ Direction, $^\circ$[a]	SWRA Bias in Speed, m s^{-1}/ Direction, $^\circ$[b]
Case 1	2.5	0.8/0.5	-1.7/0.6
Case 2	1.8	0.9/0.5	-1.2/-0.7

[a] Direction values are given in equivalent meters per second.
[b] Direction values are given in equivalent meters per second; bias sign refers to clockwise ($+$) or counterclockwise ($-$) bias.

4.2.3. Error analysis

[74] In SWRA it is assumed that SAR σ° variability may be due to speed and direction changes. The relative quality of VHR and SAR data is weighted in the analysis, taking into account the information content of the data. Nonetheless, nonlinearities in the C band model functions and inaccuracies in the cost function weights ($\Delta\sigma^2$, Δu^2, and Δv^2) introduce errors in the wind vector estimation. As described in section 3.2, the best retrieval method (minimum variance, maximum likelihood, and no bias) will depend on the errors induced by the nonlinearity of the forward model.

[75] In order to estimate nonlinearity errors in the SWRA, the following error analysis is performed. Using a true wind vector (u_t, v_t), we apply the C band model function to get a true radar backscatter σ_t° at a mean incidence angle of 23°. Then, we add the Gaussian noise corresponding to the values of Δu, Δv, and $\Delta\sigma$ discussed in section 4.2.1 to generate the VHR wind vectors $v_H^i = (u_t^i, v_t^i)$ and the backscatter measurements $\sigma_m^{\circ i}$. For each pair $[v_H^i \ \sigma_m^{\circ i}]$, we compute an SWRA wind vector (see section 4.2.1). Finally, we compute the bias of SWRA winds with respect to the true wind in speed and direction components.

[76] This procedure is performed for different true wind speeds and directions, ranging from 5 to 15 m s^{-1} (step size of 5 m s^{-1}) and from 0° to 180° (step size of 10°) (note that the rest of the angles is not computed because of symmetry).

[77] Figure 4 shows the wind speed and direction bias results in the SWRA. A positive bias in wind speed component denotes an underestimation of the SWRA with respect to the true wind speed and vice versa. Both a positive direction bias in the 0°–90° range of true wind directions and a negative bias in the 90°–180° range denote a bias toward crosswind (0° is upwind). In contrast, both a negative direction bias in the 0°–90° range and a positive direction bias in the 90°–180° range denote an upwind/downwind bias.

[78] The biases in wind speed component are always positive, denoting underestimation, and have a maximum around crosswind directions. Moreover, the underestimation increases with decreasing wind speeds. At 5 m s^{-1} for near crosswind direction it is quite a significant underestimation (0.65 m s^{-1}).

[79] The biases in the wind direction component are lower than in the speed component and are mostly toward crosswind directions. The maximum value is at low speeds and directions ranging from 50° to 60° and from 110° to 130° (equivalent to 0.31 m s^{-1}).

[80] These results indicate a systematic bias in the SWRA derived wind fields toward lower wind speeds and crosswind directions due to effects of nonlinearity. The bias is most significant in the speed component at low speeds and
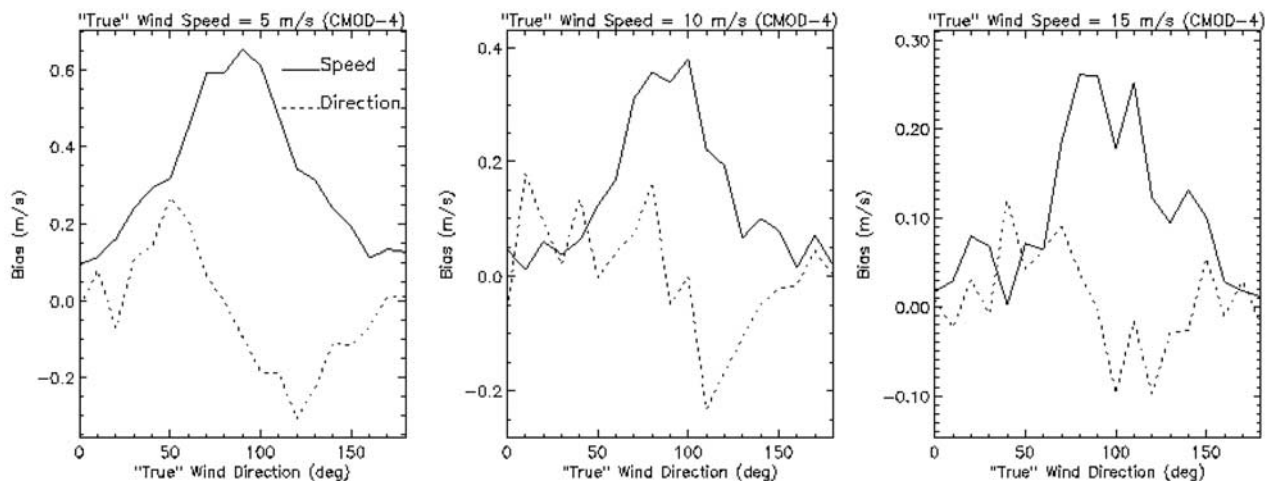
Figure 4. Bias in SWRA speeds (solid lines) and equivalent directions in meters per second (dashed lines) as a function of true wind direction for true wind speeds (a) 5 m s^{-1}, (b) 10 m s^{-1}, and (c) 15 m s^{-1}.

crosswind directions. We believe that the errors are not substantial and that the selection of the maximum likelihood (basis of the SWRA) is appropriate. We expect that if stronger assumptions than in SWRA (like assuming no error, in the method presented in section 4.1.1) are used in the SAR retrieval, then these biases will generally increase (unless specifically controlled).

5. Conclusions

[81] The potential of combining SAR backscatter data and HIRLAM wind information in mesoscale meteorological studies for coastal regions is shown to be very promising.

[82] In SAR, a single $\sigma°$ measurement is sensitive to, at least, two geophysical parameters, the wind speed and the wind direction. Therefore, an underdetermination problem occurs when retrieving winds from SAR backscatter data. Moreover, inversion is complicated by the nonlinear relationship between the backscatter and the wind.

[83] The combination of the SAR image streak information (SWDA) with the SAR backscatter information (C band model) determines a solution of the problem, but does not take account of the difference in spatial context of the SAR $\sigma°$ and the wind streak information. Moreover, uncertainties in wind streak determination and $\sigma°$ are not explicitly used in the wind interpretation.

[84] In addition, the following uncertainties have been reported from the SWDA: (1) The direction of the local wind is not detected in all the wind cases; (2) the accuracy of the method decreases with increasing wind streak spacing; and (3) the wind streaks show some misalignment either to the right or to the left of the true wind direction. The C band model derived wind speed errors are directly affected by the error in the SWDA-derived direction.

[85] In contrast, the more general inversion methodology, commonly used in meteorological analysis, can be applied to overcome such problems of underdetermination and nonlinearity. The statistical wind retrieval approach allows the retrievals of an optimum wind vector from the best combination of SAR and VHR wind information, assuming Gaussian noise errors in both "measurement" sources. The

SWRA results in a compromise between SAR and VHR information and distributes the SAR signal variability in a predefined way between speed and direction changes, according to their respective sensitivities.

[86] The SWRA shows promising results, although in particular cases the wind direction may draw closely to the VHR model output, due to relatively low SAR wind direction sensitivity. An error analysis is performed, and a systematic bias with respect to the true wind is found in both wind components. The major bias is produced at low wind speeds for crosswind directions where the SWRA underestimates the true wind speed by 0.65 m s^{-1}. Inaccuracies in the estimation of the cost function weights ($\Delta\sigma^2$, Δu^2, and Δv^2), or even in the cost function specification are identified as the main sources of error in the SWRA. Nevertheless, from a theoretical point of view the SWRA will result in a better wind analysis than the SWDA + CMOD-4.

[87] The validation study has been restricted to only 15 ERS-2 SAR images. Therefore further validation of the SWDA + C band wind field retrievals from SAR images is necessary to fully explore the impact of oceanic and atmospheric phenomena other than wind in the retrievals, not only at 5 km but also at higher resolutions. *Fetterer et al.* [1998] conclude that SWDA has the potential to retrieve directions at higher resolution, although this has not been tested yet. In that sense, higher resolution NWP models like GESIMA (1 km) or FITNAH (1.5 km) could also be more useful for validation in some cases.

[88] Further examination of the SWRA is also needed. In particular, more sophisticated estimation of the cost function weights is required in order to improve the quality of the SWRA winds. Backscatter sensitivity to wind is variable; that is, nonlinear effects can occur in the inversion that need to be further investigated. Information from wind streaks may be incorporated in the SWRA after further study of their quality and spatial representation. A higher resolution SWDA may also help to improve the quality of the SWRA. With respect to background information, more aspects like spatial background error correlation could be implemented.

[89] In view of the Envisat payload, which is not including a wind scatterometer, it is therefore attractive to improve

and develop an independent SAR wind vector retrieval method. In this context it should therefore be emphasized that ESA recently initiated the investigation, development, and testing of a new approach. This SAR wind field retrieval method is based on the consideration of the time decorrelation and phase spectra computed from interlook processing of single-look-complex (SLC) SAR data [*Johnsen et al.*, 1999]. With the use of this method, there is less demand or need for auxiliary information such as that obtained from a high-resolution atmospheric boundary layer model or from direct wind field observations. However, it does require the availability of SLC data, which demands special processing techniques.

[90] Although the SWRA also works with incomplete wind vector information, SAR independent wind vectors could also be used in the SWRA after characterization of their relative errors and could subsequently improve the quality of the SWRA wind vectors. Note also that via integrated use of SAR observations and model output (i.e., HIRLAM) in real time, the initial wind field conditions can be optimized, leading to further improvements in model prediction.

References

Alpers, W., Measurement of mesoscale oceanic and atmospheric phenomena by ERS-1 SAR, *Radio Sci. Bull.*, *275*, 14–22, 1995.

Alpers, W., and B. Brummer, Atmospheric boundary layer rolls observed by the synthetic aperture radar aboard the ERS-1 satellite, *J. Geophys. Res.*, *99*, 12,613–12,621, 1994.

Alpers, W., U. Pahl, and G. Gross, Katabatic wind fields in coastal areas studied by ERS-1 synthetic aperture radar imagery and numerical modeling, *J. Geophys. Res.*, *103*, 7875–7886, 1998.

Brown, R. A., Surface fluxes and remote sensing of air-sea interactions, in *Surface Waves and Fluxes*, edited by G. L. Geernaert and W. J. Plant, pp. 7–27, Kluwer Acad., Norwell, Mass., 1990.

Chapron, B., T. E. Fouhaily, and V. Kerbaol, Calibration and validation of ERS wave mode products, *DRO/OS/95-02*, Inst. Fr. de Rech. pour l'Exploit. de la Mer, Brest, France, 1995.

De Bruijn, E. I. F., Experiments with horizontal diffusion and advection in a nested fine mesh mesoscale model, internal report, K. Ned. Meteorol. Inst., De Bilt, Netherlands, 1997.

Etling, D., and R. A. Brown, Roll vortices in the planetary boundary layer: A review, *Boundary Layer Meteorol.*, *65*, 215–248, 1993.

Fetterer, F., D. Gineris, and C. Wackerman, Validating a scatterometer wind algorithm for ERS-1 SAR, *IEEE Trans. Geosci. Remote Sens.*, *36*(2), 479–492, 1998.

Gerling, T. W., Structure of the surface wind field from the Seasat SAR, *J. Geophys. Res.*, *91*, 2308–2320, 1986.

Grabak, O., and H. Laur, ERS SAR.PRI CCT and Exabyte, *ER-IS-EPO-GS-5902.4*, Eur. Space. Agency, Paris, France, 1995.

Gudiksen, P. H., J. M. Leone, C. W. King, D. Ruffieux, and W. D. Neff, Measurements and modelling of the effects of ambient meteorology on nocturnal drainage flows, *J. Appl. Meteorol.*, *31*, 1023–1032, 1992.

Gustafsson, N., The HIRLAM model, in *Seminar Proceedings on Numerical Methods in Atmospheric Models*, vol. 2, pp. 115–146, Eur. Cent. for Medium-Range Weather Forecasts, Reading, England, 1991.

Institut Français de Recherche pour l'Exploitation de la Mer, WNF products: User manual, *C2-MUT-W-01-IF*, Brest, France, 1996.

Johannessen, J. A., R. Schuchman, O. M. Johannessen, and K. Davidson, Synthetic aperture radar imaging of ocean circulation features and wind fronts, *J. Geophys. Res.*, *96*, 10,411–10,422, 1991.

Johannessen, J. A., P. W. Vachon, and O. M. Johannessen, ERS-1 SAR imaging of marine boundary layer processes, ESA EOQ 46, Eur. Space Agency, Paris, France, 1994.

Johannessen, J. A., P. W. Vachon, and O. M. Johannessen, ERS-1 SAR imaging of marine boundary layer processes, study of Earth system from space, *J. Earth Obs. Remote Sens.*, (Russian), *3*, 1996.

Johnsen, H., G. Engen, K. Hogda, B. Chapron, and Y. Desnos, Validation of Envisat ASAR wave mode level 1b and level 2b products using ERS SAR data, *ESA SP-450*, pp. 59–64, Eur. Space Agency, Paris, 1999.

Kerbaol, V., B. Chapron, and P. W. Vachon, Analysis of ERS-1/2 synthetic aperture radar wave mode imagettes, *J. Geophys. Res.*, *103*, 7833–7846, 1998.

Korsbakken, E., J. A. Johannessen, and O. M. Johannessen, Coastal wind field retrievals from ERS synthetic aperture radar images, *J. Geophys. Res.*, *103*, 7857–7874, 1998.

Laur, H., P. Bally, P. J. Meadows, J. Sanchez, B. Schaettler, and E. Lopinto, ERS SAR calibration: Derivation of the backscattering coefficient s° in ESA ERS SAR PRI products, *ESA/ESRIN ES-TN-RS-PM-HL09 2*, rev. 5, Eur. Space Agency, Paris, 1998.

Lehner, S., J. Horstmann, W. Koch, and W. Rosenthal, Mesoscale wind measurements using recalibrated ERS SAR images, *J. Geophys. Res.*, *103*, 7847–7856, 1998.

LeMone, M. A., Structure and dynamics of horizontal roll vortices in the planetary boundary layer, *J. Atm. Sci.*, *30*, 1077–1091, 1973.

Lorenc, A. C., Analysis methods for numerical weather prediction, *Q. J. R. Meteorol. Soc.*, *112*, 1177–1194, 1986.

McNider, R. T., and R. A. Pielke, Numerical simulation of slope and mountain flows, *J. Appl. Meteorol.*, *23*, 1441–1453, 1984.

Mesinger, F., and A. Arakawa. Numerical methods used in atmospheric models. GARP Publ. Ser. 17, vol. 1, 64 pp., World Meteorol. Org./Int. Counc. of Sci. Unions Joint Organising Committee, Geneva, 1976.

Pond, S., and G. L. Pickard, Introductory Dynamic Oceanography, edited by Pergamon, New York, 1978.

Portabella, M., ERS-2 SAR wind retrievals versus HIRLAM output: A two way validation-by-comparison, *Internal Rep. EWP-1990*, Eur. Space Res. and Technol. Cent., Noordwijk, Netherlands, 1998.

Scoon, A., I. S. Robinson, and P. J. Meadows, Demonstration of an improved calibration scheme for ERS-1 SAR imagery using a scatterometer wind model, *Int. J. Remote Sens.*, *17*(2), 413–418, 1996.

Stoffelen, A., Error modelling of scatterometer in-situ, and ECMWF model winds; A calibration refinement, *Tech. Rep. TR-193*, K. Ned. Meteorolog. Inst., De Bilt, Netherlands, 1996.

Stoffelen, A., Toward the true near-surface wind speed: Error modeling and calibration using triple collocation, *J. Geophys. Res.*, *103*, 7755–7766, 1998.

Stoffelen, A., A generic approach for assimilating scatterometer observations, paper presented at ECMWF Seminar on Exploitation of the New Generation of Satellite Instruments for Numerical Weather Prediction, Eur. Cent. for Medium-Range Weather Forecasting, Reading, UK, 2000.

Stoffelen, A., and D. L. T. Anderson, ERS-1 scatterometer data and characteristics and wind retrieval skill, *Eur. Space Agency Spec. Publ., SP*, *359*(1), 41–47, 1992.

Stoffelen, A., and D. Anderson, Scatterometer data interpretation: Estimation and validation of the transfer function CMOD-4, *J. Geophys. Res.*, *102*, 5767–5780, 1997a.

Stoffelen, A., and D. Anderson, Scatterometer data interpretation: Measurement space and inversion, *J. Atmos. Oceanic Technol.*, *14*(6), 1298–1313, 1997b.

Vachon, P. W., and F. W. Dowson, Validation of wind vector retrieval from ERS-1 SAR images over the ocean, *Global Atmos. Ocean Syst.*, *5*, 177–187, 1996.

Valenzuela, G. R., Theories for interaction of electromagnetic and oceanic waves: A review, *Boundary Layer Meteorol.*, *13*, 61–85, 1978.

Wackerman, C., C. Rufenach, R. Schuchman, J. Johannessen, and K. Davidson, Wind vector retrieval using ERS-1 synthetic aperture radar imagery, *IEEE Trans. Geosci. Remote Sens.*, *34*, 1343–1352, 1996.

————————
J. A. Johannessen, Nansen Environmental and Remote Sensing Center (NERSC), Edvard Griegsvei 3a, 5059 Bergen, Norway. (johnny.johannessen@nrsc.no)

M. Portabella and A. Stoffelen, Royal Netherlands Meteorological Institute (KNMI), Postbus 201, 3730 AE De Bilt, The Netherlands. (portabel@knmi.nl; Ad.Stoffelen@knmi.nl)